

## Positive-Pion Production in Inelastic $\pi^-p$ Interactions between 500 and 1300 MeV\*

DOUGLAS C. GIANCOLI,† BARRY C. BARISH,‡ SELIG N. KAPLAN, RICHARD J. KURZ,§  
VICTOR PEREZ-MENDEZ, AND JULIUS SOLOMON||

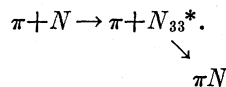
Lawrence Radiation Laboratory, University of California, Berkeley, California

(Received 19 September 1966)

The momentum distributions of the  $\pi^+$  in the reaction  $\pi^-p \rightarrow \pi^+\pi^-n$  were measured at several  $\pi^+$  angles for incident  $\pi^-$  beam energies of 516, 550, 599, 667, and 715 MeV;  $\pi^-n$  mass spectra were calculated from the  $\pi^+$  momentum distributions. Partial data were also obtained at higher energies. The  $\pi^-$  beam was obtained from the Berkeley Bevatron. The momenta of the  $\pi^+$  were measured with a magnetic spectrometer consisting of a C magnet and thin-walled aluminum spark chambers to display the trajectory of the particle entering and leaving the magnet. An array of scintillation counters was used to detect the occurrence of an event. An electronic time-of-flight system was used to distinguish positive pions from protons that passed through the spectrometer. The measured spectra can not be adequately explained by any of the several models with which we tried to fit our spectra, including an isobar model, although production of the (3,3) isobar is prominent.

### I. INTRODUCTION

THE experiment described in this paper was undertaken in the hope of contributing to knowledge of the pion-nucleon interaction in the region of the 600-MeV peak in the isotopic-spin,  $T = \frac{1}{2}$  state. In this energy region the elastic cross sections have been examined in detail, whereas the inelastic reactions have not received such thorough treatment. However, it is known that the inelastic processes are large. It is also known that the production of the  $N_{33}^*$  is important in these inelastic reactions, i.e.,



This experiment was designed to study this type of final state. In particular, we examine the reaction  $\pi^-p \rightarrow \pi^+\pi^-n$  in the region of the 600-MeV peak and measure the  $\pi^+$  energy spectra (equivalent to the  $\pi^-n$  mass spectra) at various (discrete) angles.

This reaction was chosen because (a) the  $\pi^+$  is a unique signature among  $\pi\pi N$  states, and (b) the Clebsch-Gordan coefficients indicate that in the  $T = \frac{1}{2}$  state, at least, the  $\pi^-n$  combination can form an  $N_{33}^*$  isobar much more often than can  $\pi^+n$ —thus the  $\pi^-n$  mass spectra should show a significant peaking at a mass corresponding to a recoiling  $N_{33}^*$ , if it is formed.

A plot of the kinematics (see Fig. 1) indicates that at a given  $\pi^+$  angle in the laboratory system, the  $\pi^-n$  mass distribution at a nearly constant center-of-mass angle is observed.

\*Work done under auspices of the U. S. Atomic Energy Commission.

† Present address: National Institute of Health Fellow in Department of Molecular Biology, University of California, Berkeley, California.

‡ Present address: California Institute of Technology, Pasadena, California.

§ Present address: Space Sciences Division, Goddard Space Flight Center, Greenbelt, Maryland.

|| Present address: University of Illinois at Chicago Circle, Chicago, Illinois.

Measurements of spectra were made extensively in the region from 516–715-MeV incident  $\pi^-$  kinetic energy. A limited amount of data was also taken at higher energies. In these latter spectra, however, we present only the combined recoil mass spectra of all final states that contain a  $\pi^+$ ; this is because of the significant yields of multipion production states at these higher energies for which we could not correct. A summary of the experimental conditions is given in Table I.

A more detailed account of the experimental aspects can be found in Ref. 1.

### II. EXPERIMENTAL METHOD AND APPARATUS

A monoenergetic ( $\pm 2.5\%$ ) beam of negative pions, produced by the Berkeley Bevatron, was transported to the experimental area by the magnetic system shown

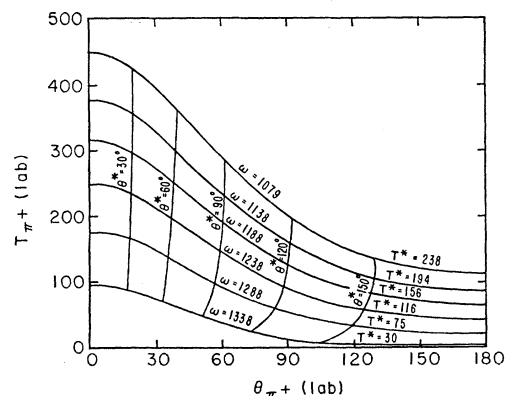
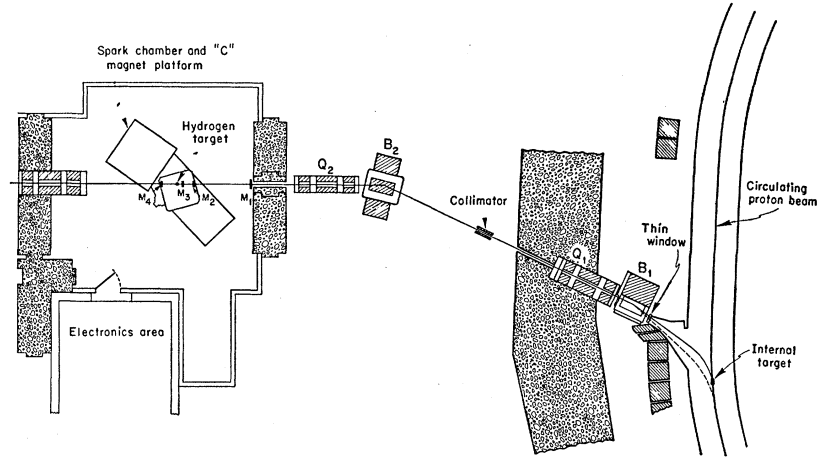


FIG. 1. Pion kinematics for  $\pi^-p \rightarrow \pi^+\pi^-n$  at an incident energy of 599 MeV. The solid lines represent lines of constant c.m.  $\pi^+$  angle ( $\theta^*$ ) and  $\pi^-n$  recoil mass ( $\omega$ ) [equivalent to c.m. kinetic energy of the  $\pi^+$  ( $T^*$ )] as labeled.  $T_{\pi^+}$  (lab) refers to the laboratory kinetic energy of the  $\pi^+$  (in MeV); and  $\theta_{\pi^+}$  (lab) is the lab angle of the  $\pi^+$  in degrees.

<sup>1</sup> Douglas C. Giancoli, Ph.D. thesis, Lawrence Radiation Laboratory Report No. UCRL-16282, 1966 (unpublished).

FIG. 2. Plan view of the experimental arrangement, including beam setup. Detail of experimental area is given in Fig. 3.



in Fig. 2. This beam, whose properties are given in Table I, was focused on a cylindrical liquid-hydrogen target of 3.75-in. diam and 5.77-in. effective length. The beam was monitored by the  $M_1$ ,  $M_2$ , and  $M_3$  scintillation counters in front of the target and  $M_4$  behind the target in anticoincidence.

The momentum spectrum of final-state positively charged particles was analyzed by a magnetic spectrometer (Fig. 3). The spectrometer magnet had 16×36-in. pole faces and an 8-in. gap. The central field was 17.8 kG—so chosen to allow simultaneous analysis of momenta between 150 and 800 MeV/c. The entrance aperture was defined by a 1.5×6× $\frac{3}{8}$ -in. scintillation

counter  $S_0$ . It was mounted immediately in front of the magnet, 41 in. from the center of the liquid-hydrogen target. Position and direction of the entrance track was precisely determined with an eight-gap 6×12×6-in. spark chamber placed ahead of counter  $S_0$ . To ensure precise determination of incident direction, a heavy iron shield was necessary between the entrance spark chamber and the magnet to reduce the field in the chamber to less than 300 G.

A positive particle's exit from the spectrometer was indicated by one of the seven counters,  $S_1, \dots, S_7$ , and position was precisely determined with two six-gap 12×40×2-in. spark chambers (Fig. 3). The spectrometer sat on a rotating gun mount whose axis of rotation was at the center of the hydrogen target.

Two mutually perpendicular views of each chamber were projected by a lens and mirror system onto the

TABLE I. Experimental conditions.<sup>a</sup>

Incident $\pi^-$ kinetic energy (MeV)	Spectrometer lab angles (deg)	Beam contamination (%)		
		Elec- trons	Muons	Total
516	18, 37, 60, 88	24.0	17.5	41.5
550	18, 37, 60, 74.5, 88	21.0	17.2	38.2
599	18, 37, 48, 60, 74.5, 88, 105	17.0	11.3	28.3
667	18, 37, 60, 88	15.5	11.7	27.2
715	18, 37, 48, 60, 74.5, 88	12.7	15.6	28.3
890	37, 60	15.0	8.7	23.7
1008	60	15.8	5.7	21.5
1118	37, 60	12.5	7.5	20.0
1329	60	8.0	5.9	13.9
Other beam properties				
Energy spread, $\Delta T/T$ (trapezoidal, HWHM)	2.5%			
Angular distribution (FWHM, all energies)	horizontal: 2 deg vertical: 1.25 deg			
Spatial distribution (FWHM, all energies)	horizontal: $2.1 \pm 0.15$ in. vertical: $2.2 \pm 0.15$ in.			
Duration of beam pulse	200 to 800 msec			
Average instantaneous rate at our target	$2 \times 10^6$ pion/sec			

<sup>a</sup> Four basic angles (18, 37, 60, and 88 deg) were run at the five lower energies. These four angles correspond, at all these energies, to  $\pi^-n$  production angles close to 150, 120, 90, and 60 deg. The other angles (48, 74.5, and 105 deg, corresponding to  $\pi^-n$  production angles of, respectively, 105, 75, and 45 deg) at some energies generally have poorer statistics. The c.m. angle varies slightly as a function of pion momentum (within 3 deg except for the very lowest pion momenta). The angular acceptance of the spectrometer is 4.2 deg (lab).

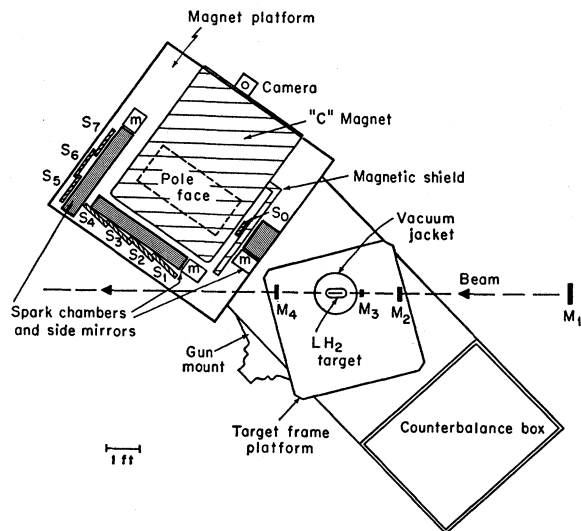


FIG. 3. Diagram of experimental area, showing spectrometer and monitor system. The beam-monitor counters ( $M_1, M_2, M_3, M_4$ ) are not shown to scale. The letter  $m$  refers to side mirrors on the spark chambers, and  $S_i$  are the spectrometer counters.

focal plane of a double-frame 35-mm camera. A scribed Lucite grid on each chamber face was illuminated between beam pulses by a fluorescent lamp. In addition, two neon fiducial lamps on each face were pulsed for every event.

To provide a basis for momentum determination, a detailed magnetic-field map was made. Our momentum-determination procedure (see Sec. III) was checked by using the suspended-wire technique and by measurement of elastic proton peaks and elastic  $\pi^-$  peaks (with the field reversed). Agreement was within 1%. The momentum resolution of the system,  $\Delta p/p$ , varied from 5.5% at low momentum to 2% at high momentum. This variation arose from uncertainties in the energy loss in material between the point of interaction and the spectrometer, and from multiple scattering, momentum-estimation procedure, and scanner-measurement error.

Since low-momentum particles are deflected too much to pass through an exit spark chamber and counter, we calculated the efficiency of the spectrometer as a function of momentum by averaging over the possible entrance trajectories. This gave the efficiency for pions,  $\epsilon$ , to be

$$\begin{aligned} \epsilon &= 0 && \text{for } p < 122 \text{ MeV}/c, \\ \epsilon &= (p - 122)/50 && \text{for } 122 \text{ MeV}/c \leq p \leq 172 \text{ MeV}/c, \\ \epsilon &= 1 && \text{for } 172 \text{ MeV}/c > p. \end{aligned}$$

A 10-kV pulse was sent to the spark chambers to activate them after occurrence of a coincidence between a  $\pi^-$  interaction in the target and a positive-particle traversal of the spectrometer (indicated by an  $M_1 M_2 M_3 \bar{M}_4 S_0 S_i$  coincidence, where  $S_i$  is any one of the  $S_1, \dots, S_7$  spectrometer exit counters). The total time delay from particle passage to spark-chamber activation was less than 400 nsec.

Since we were interested in the spectrum of  $\pi^+$ , some method of separating pions from protons was necessary. This was achieved by time-of-flight measurements using the time difference between a beam particle passing  $M_1$  and a positive particle traversing  $S_0$ . This time difference was measured by a time-to-height converter whose output signal was sent to an analog-to-digital converter. The resolution of the time-of-flight system,  $\pm 1.5$  nsec, was sufficient to separate pions from protons, since in the worst case (highest momentum) the difference in transit time of pions and protons was 3 to 4 nsec. With this resolution it was not possible to separate muons or positrons. Periodically, the spectrometer was rotated into the beam (0 deg) and a timing measurement was made on the beam particles in order to check the calibration of our timing system. We found the long-term stability of the system to be better than  $\frac{1}{3}$  nsec.

A data-accumulation system accepted the digitized time-of-flight information and the number of the exit counter through which the particle passed, and assigned a five-digit (octal) identification number. These data

were then transferred both to magnetic tape (through an intermediate buffer storage) and to a neon-light data box that was viewed by the spark-chamber camera through a half-silvered mirror and lens system. (A typical spark-chamber picture, including the data box lights, is shown in Fig. 4.) At the beginning of each run, coded run-identification and running-condition information was put on the magnetic tape. At the end of each run, the accumulated counts of beam- and event-monitor scalers were read out onto the tape.

### III. DATA ANALYSIS

#### A. General Analysis

##### 1. Film Measurement and Data Reduction

The film was measured with a semiautomatic digitizing protractor. All the information for each measured event, including the run number, event number, and other fixed data, as well as the digitized measurements, was recorded on tape. Both views of each track, plus two fiducial points, were measured. If the event was not considered measurable because of the absence of one or both tracks, a duplicity of tracks, scattering of the particle in a spark chamber, or the poor quality of a picture, then an appropriate code number was recorded for the event. The  $S_i$  counter number that appeared on the film was not only useful for locating the exit track quickly but also was used to distinguish which of two exit tracks (a two-track event occurred occasionally) was the correct one.

Spatial orientation of the fiducial points, and therefore of the tracks, was ultimately determined by referencing to the illuminated grids. These grids also were used to correct for distortions introduced by lenses in both experimental and scanning systems. A series of measurements of these grids was made regularly. From these measurements a computer program calculated the various distances and angles associated with the grids and fiducial points. These were later used in deciphering each event measurement.

A second computer program calculated the following quantities for each measured event.

(a) *The particle momentum.* This was determined in the following way: From the measured entrance and exit tracks of a given event and a simplified representation of the magnetic field, an approximate momentum,  $P_1$ , was estimated. By use of the measured entrance track, the map of the magnetic field, and  $P_1$  as the momentum, an orbit was traced. The exit position of this hypothetical orbit was used to calculate another momentum estimate,  $P_2$ . The momentum was then reestimated to be

$$P = P_1 - (P_2 - P_1) = 2P_1 - P_2.$$

A second orbit, traced for a number of events of various types, showed that the above procedure gave the momentum in all cases to  $\Delta p/p \leq 0.5\%$ .

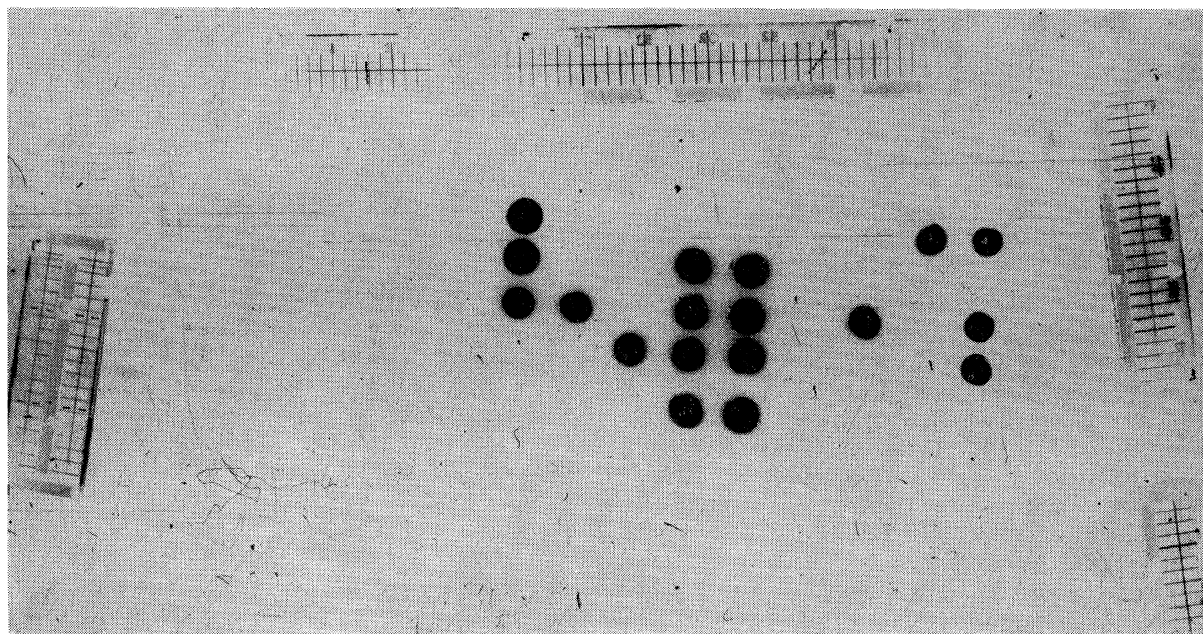


FIG. 4. A typical event photograph of the particle tracks in the spark chambers surrounding the spectrometer magnet. The spark chamber at the left was at the entrance to the magnet. Although the spark chambers were at right angles to one another, on the film they do not appear that way because of the characteristics of our optical mirror system. The large numbered dots in the center are the data box lights, which indicate the frame number, timing information, and  $S_i$  counter number.

(b) *Exit-angle difference.* Since only the particle's entrance position and direction and exit position were needed to determine the momentum, the measured exit direction could be compared with that predicted for the orbit of a particle of a particular momentum.

(c) *Exit-height difference.* The vertical position of the exit track could be predicted (by calculation) from the vertical entrance position and angle; this was compared with the measured exit vertical height.

(d) *Distance between fiducial points.* This was actually a ratio of the measured value to the average value.

(e) *Point of interaction in the target.* The entrance track, both horizontal and vertical views, was extrapolated to its intersection with a vertical plane along the central beam line (exact position of a beam particle was not known).

(f) *Angle of scattering.* This was the angle of the spectrometer plus the small angle of the particle with respect to the spectrometer.

Items (b) and (c) were used to check whether the particle had decayed, scattered, or otherwise did not have a normal orbit, or if the event were poorly measured; (d) was a check against a poor measurement or machine malfunction.

A library tape was generated which included all the above information for every event as well as the time of flight, a number representing the scanner who measured the event, picture-quality code number,  $S_i$  detector number, and the momentum. Each event on this tape was checked to see whether or not it fitted certain

criteria with regard to (b), (c), and (d). If an event did not fit all the criteria, or if it were coded (i.e., not measurable) it was later carefully rescanned and remeasured. All other events were measured only once except for several samples of events which were measured by several or all scanners for a scanner-consistency check.

## 2. Data Analysis

Pions and protons were separated by comparing time of flight with momentum. Less than 0.5% of the events were ambiguous—and therefore rejected.

For events selected as pions, the c.m. kinetic energy of the  $\pi^+$  was calculated, using the angle of scattering and correcting for the energy lost by the particle as it went from the target to the spectrometer.

After all the events were categorized, a consistency check of all the several hundred runs was made.

A computer program was written which calculated the following quantities and averaged them over all the runs for each experimental condition: percentages of  $\pi$  events, proton events, ambiguous events, coded events, events not target-derived, events not meeting exit-angle and height criteria, and the  $\pi^+$  spectra (divided into only three energy intervals to obtain better statistics). With the averages at each condition calculated, each run was compared with the average for all runs at that condition and

$$\chi^2 = (X - \bar{X})^2 / (\text{statistical error})^2$$

was calculated. The distribution in  $\chi^2$  for each quantity,

and for all experimental conditions, was plotted. It was found to follow the expected  $\chi^2$  distribution quite well. We therefore decided that the data were consistent, except for one run which had an extraordinarily low number of protons; it was judged questionable and deleted. This procedure was followed for both full and empty target.

A similar calculation in which the five scanners were compared revealed no significant inconsistencies.

In order to determine if any areas of our exit spark chambers were less than 100% efficient, the scanners were instructed to use a special code for an event if any of the tracks they measured were questionable, that is, if the scanner felt he could not measure a track to within certain specified criteria—namely, (a) the position of a good exit track should be known to within 0.1 in. in real space (measured with respect to the 1-in. grid marks on the spark-chamber grid), and (b) its angle should be known to within 3 deg. These criteria would give the momentum to less than 1% error. We plotted these coded events as a function of exit chamber position, which was roughly proportional to momentum, and found that this type of event accounted for less than 3% of the events in any region of the spark chambers. On this basis, we assumed that within the statistics of our data (on the order of 10%) the spark chambers exhibited no bias.

After all the events were on the library tape and the bad runs were deleted, the spectra were calculated. However, certain criteria were applied to each event in order to reduce the background. With reference to the quantities (b) through (f) mentioned in Sec. III.A.1, events that did not meet the following criteria, even after remeasurement, were rejected: (b) exit-angle difference less than 5 deg, (c) exit-height difference less than 4 in., and (d) distance between the fiducial points within 1% of the calculated average. A plot of (b) and (c) for a large number of events is shown in Fig. 5. The cutoffs mentioned above were chosen because the muon-contamination calculation (Sec. III.B.2) indicated that nearly all events outside the cutoffs were decay muons. This is not critical, however, because only 0.5% of the events fell outside these cutoffs. The 1% cutoff for (d) was rather arbitrary; however, an error of this magnitude had very little effect on the measured quantities. Because most bad measurements were remeasured, only 0.01% of the events were deleted by this test. In addition, (e) was used to require that the interaction have taken place in the target. As noted earlier, the point of interaction, as given in (e), was calculated with the beam particle assumed to be on the center line of the target. Of course, this was not usually the case, because the beam had a finite extension in space. Therefore, the true point of interaction could be different from that given in (e). The distribution of events, according to the calculated points of interaction in the target, was plotted for both full and empty target. As an example, Fig. 6 shows the results for events at all

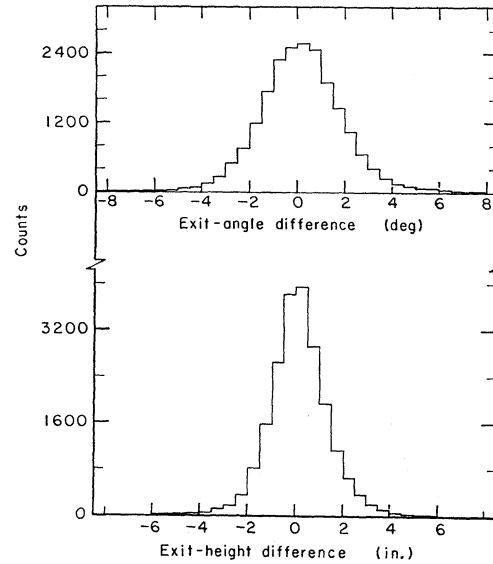


FIG. 5. Top: Histogram of the difference between the actual exit angle and the exit angle calculated from the orbit, for a large number of events (see text). Bottom: Histogram of the difference between the actual exit height and the exit height calculated from the entrance track and the orbit of the particle, for a large number of events (see text).

incident momenta at 18 deg, the worst case, and also at 60 deg.

In order to calculate the normalization for each spectrum, it was necessary to be sure to include all particles which interacted in the hydrogen, and then to

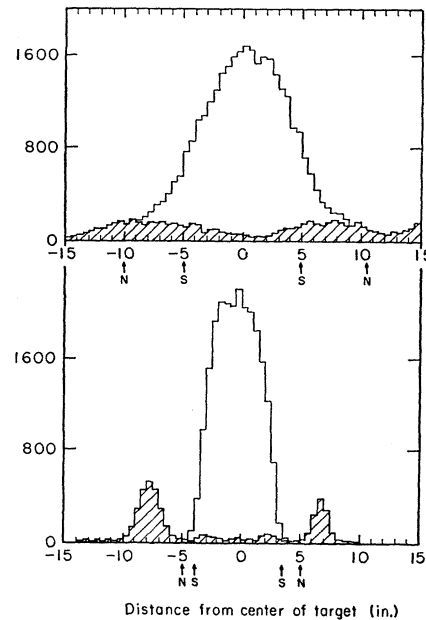


FIG. 6. Two histograms of the calculated point of interaction in the target (see text). The top is for the spectrometer set at 18 deg, the bottom at 60 deg. "N" and "S" refer to the cutoffs used for normalization and spectra, respectively. The shaded areas refer to the empty-target (i.e., background) spectrum.

subtract the background (determined from empty runs); in addition, for best statistics, the full-to-empty ratio should be kept as large as possible consistent with the above. As shown in Fig. 6, beyond a certain distance from the target center in both directions the numbers of full and empty counts become (statistically) equal; thus we can assume that none of these events are hydrogen-derived. Cutoffs (indicated by "N" in Fig. 6) were then chosen just beyond this point of equality, and only events within these cutoffs were included in the normalization calculation.

To determine the shape of the  $\pi^+$  energy distribution, absolute normalization was not necessary. With the smaller number of events in each energy interval, it was highly desirable to maximize the full-to-empty ratio as far as possible to obtain the best statistics; i.e., we wanted as "clean" a sample as possible. By carefully choosing the cutoffs, the relative background could be greatly reduced; these cutoffs are indicated in Fig. 6 by "S."

The selection in the target-height variable was less critical and was chosen to be  $\pm 3$  in. for the normalization (to be sure to include all interactions in hydrogen) and  $\pm 2$  in. for the spectra.

## B. Corrections

Each of the following corrections was made by use of a Monte Carlo calculation.

### 1. Positron Contamination

Since it was impossible to separate positrons from pions with our timing system, the positron contamination in our spectrometer had to be calculated. The principal source of positrons was the decay of neutral pions.<sup>2</sup> Both one- and two-pion final states were included in the calculation.

We computed the separation of each  $e^+e^-$  pair,<sup>3,4</sup> taking into account multiple scattering, and accepted as contamination those events that appeared as a single track in the entrance chamber. There are three ways in which a positron would be recorded as a good event: (a) if the two particles were sufficiently separated that the positron passed through the spark chamber and the electron missed, (b) if the two were sufficiently close together to appear as one (a separation of at least 0.1 in. was required for the scanners to resolve two tracks), (c) if both  $e^+$  and  $e^-$  passed through the entrance chamber but only one was recorded because of multiple-spark inefficiency of the spark chamber.

The positron spectra obtained were weighted by our magnet efficiency and then subtracted from the raw

data. The positron contamination at each angle and beam energy decreased as a function of positron momentum. As a function of angle of the spectrometer, the contamination varied from about 10% at the most forward angle to less than 1% at the backward angles. The sources of error in this calculation were the uncertainty in the  $\pi^0$  production cross sections, and the uncertainty in the 0.1-in. measurability cutoff in the separation of the electron-positron pair. If this cutoff was increased by a factor of 2 (an extreme upper limit) the correction was changed by about 20%. Even then the total error in this calculation was somewhat less than the statistical error on the original data points.

### 2. Pion Decay

After the positron correction, we assumed that only pions and muons contribute to the spectra. The muons arise from the decay of pions. The fraction of pions directed toward the spectrometer but lost due to decay was calculated as a function of the pion momentum. Most of the positive muons produced in these decays did not traverse the spectrometer or were not accepted on the basis of the special entrance and exit requirements (see Sec. III.A.1).

The remaining decay muons were indistinguishable from pions and hence constituted a contamination of the observed spectra. The apparent momentum distribution in the spectrometer of these muons was calculated. The total correction was then normalized as a function of momentum by using the observed spectra. The correction varied from 15% at low momentum to 5% at high momentum, and therefore renormalization to the corrected spectra was not considered necessary. Finally, the contribution due to the decay of pions not directed toward the spectrometer was calculated and found to be negligible.

### 3. Pion Scattering

The spectra obtained after we corrected our raw spectra for the two previous contaminations were assumed to contain only pions. However, a certain fraction of the pions which were originally heading for the spectrometer was scattered away by nuclear scattering in the material between the original interaction and the  $S_0$  counter. In addition, a correction was necessary for those pions which although not originally headed for the spectrometer were scattered into it, thus contaminating our spectra. The production of positive particles by  $\pi^-$  interactions in the  $S_0$  counter was calculated and found to give less than 1% contamination in the worst case. The first two effects were treated separately, and are discussed under (a) and (b) following.

(a) The calculation of the pions lost due to scattering was much like that for the muon contamination, in that it was necessary to calculate the ratio of  $\pi^+$  that scatter to those that do not, and then to normalize to our spectra. Pions were traced from the center of the hydro-

<sup>2</sup> Charles B. Chiu, Ph.D. thesis, Lawrence Radiation Laboratory Report No. UCRL-16209, 1965 (unpublished).

<sup>3</sup> W. Heitler, *The Quantum Theory of Radiation* (Oxford University Press, Cambridge, 1954) 3rd ed.; Hans A. Bethe and Julius Ashkin, in *Experimental Nuclear Physics*, edited by E. Segrè (John Wiley & Sons, Inc., New York, 1953), Vol. 1.

<sup>4</sup> R. H. Dalitz, Proc. Phys. Soc. (London) **A64**, 667 (1951).

gen target through the liquid hydrogen, aluminum, and  $S_0$  counter, all of which could cause scattering.

The total cross section for  $\pi^+p(H_2)$  is well known, but for Al and C, we used the Sternheimer optical model<sup>5</sup> with the effective radius  $R=1.42A^{1/3}\times 10^{-13}$  cm, which is in good agreement with the experimental data (e.g., see Lindenbaum).<sup>6</sup> We assumed that if a pion scattered, it was lost; this assumption was a good one because our spectrometer entrance counter, as well as exit counters, subtended a small solid angle. This scattering correction was small (a few percent) except in the region of 200-MeV  $\pi^+$  kinetic energy, where this correction was as high as 9%.

(b) Although the majority of the positive pions produced are not directed toward our spectrometer, they can rescatter, mostly elastically, and a small fraction of these head toward our spectrometer. Those that rescatter in the hydrogen appear to be good events, whereas those rescattering from other material (at some distance from the target) usually do not appear to originate in the target, and our strict criteria for a target-derived event (see Sec. III.A) reject these events. We assumed therefore that the rescattering was all  $\pi^+p(H_2)$  scattering.

#### 4. Multiple-Pion Production

Positive pions are produced not only in the reaction we are studying, but also in multiple-pion-production reactions, which are contaminants in our experiment. The available data<sup>7</sup> indicate that the only significant multiple pion production below about 700 MeV is  $\eta$  production, with a threshold at 560 MeV, where the  $\eta$  decays to  $\pi^+\pi^-\pi^0$ . This correction, therefore, was applied only at 595, 665, and 715 MeV.

The  $\eta$  was assumed to be produced isotropically in the center of mass, and the  $\pi^+$  angular distribution in the  $\eta$  rest frame was taken as isotropic. The  $\pi^+$  energy distribution in the  $\eta$  rest frame was obtained from experimental data.<sup>8</sup> The results were normalized to the total  $\eta$ -production cross section. Our c.m. energy spectra were affected only at low  $\pi^+$  energy because these  $\pi^+$  contaminants did not have as much energy available and thus could not reach the higher energies in our spectra. The correction reached 20 to 30% at the lowest  $\pi^+$  energies and decreased rapidly with increasing energy. The error associated with this correction, about 25% of the correction, was principally due

<sup>5</sup> R. M. Sternheimer, *Phys. Rev.* **101**, 384 (1956).

<sup>6</sup> S. J. Lindenbaum, *Ann. Rev. Nucl. Sci.* **7**, 317 (1957).

<sup>7</sup> Janos Kirz, Ph.D. thesis, Lawrence Radiation Laboratory Report No. UCRL-10720, 1963 (unpublished); E. Pickup, D. K. Robinson, E. O. Salant, F. Ayer, and B. A. Munir, *Phys. Rev.* **132**, 1819 (1963); W. D. Shepard and W. D. Walker, *ibid.* **126**, 278 (1962); I. Derado and N. Schmitz, *ibid.* **118**, 309 (1960); W. P. Walker, F. Hushfar, and W. D. Shepard, *ibid.* **104**, 526 (1956); W. Bruce Richards, Ph.D. thesis, Lawrence Radiation Laboratory Report No. UCRL-16195, 1965 (unpublished); Brandeis-Brown-Harvard-MIT-Padova Collaboration, *Phys. Rev. Letters* **13**, 486 (1964).

<sup>8</sup> Leroy R. Price, Lawrence Radiation Laboratory (private communication); Arthur H. Rosenfeld, Lawrence Radiation Laboratory Report No. UCRL-10492, 1962 (unpublished).

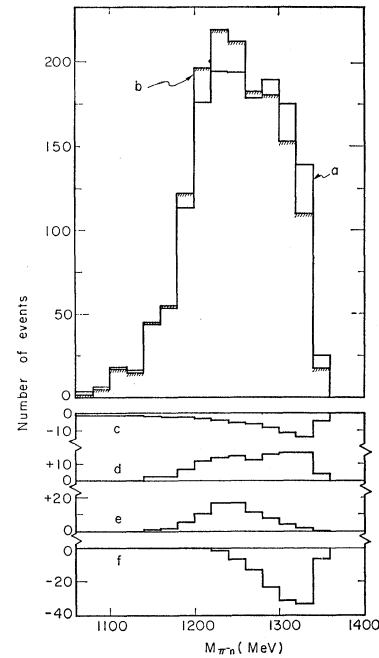


FIG. 7. Spectrum and corrections at 599 MeV and 37-deg lab angle. Histogram (a) is the raw spectrum; (b) is the corrected spectrum; (c) is the positron correction; (d) is the pion-decay correction; (e) is the  $\pi^+$  scattering correction; (f) is the correction for multipion production.

to the uncertainty in the production cross section and in the branching ratio.

In order to indicate graphically all the corrections discussed in this section, the spectrum and its corrections at 599 MeV and 37-deg lab angle are presented in Fig. 7 as an example. This particular spectrum was chosen because the magnitudes of the corrections for it were among the largest and thus easiest to see on a graph. Histogram (a) represents the raw data and histogram (b) represents the corrected spectrum. Histograms (c) through (f) represent the magnitudes of the various corrections; those which add to the spectrum are shown positive, those which subtract are shown negative.

## IV. RESULTS

The differential distributions with respect to solid angle in the c.m. frame and with respect to mass of the recoil  $\pi^-n$  system,  $d^2\sigma/d\Omega^*dM$ , were calculated. The first step was to obtain  $\Delta N/\Delta\Omega\Delta M$ , the number of events that enter the solid angle subtended by the spectrometer,  $\Delta\Omega$ , in a momentum interval that corresponds to a 20-MeV-wide  $\pi^-n$  recoil mass interval. (The selection of events has been described in Sec. III.A.) Next, transformation to the c.m. system was carried out for each event. Because  $d\Omega/d\Omega^*$  is a function of momentum and angle, it was calculated for each event, and then the average for each recoil-mass bin,  $\langle d\Omega/d\Omega^* \rangle$ , was calculated. Thus,

$$\frac{\Delta N}{\Delta\Omega^*\Delta M} = \frac{\Delta N}{\Delta\Omega\Delta M} \langle d\Omega/d\Omega^* \rangle.$$

The corrections discussed in Sec. III.B were applied to obtain  $\Delta N$ .

To obtain  $d^2\sigma/d\Omega^*dM$ ,  $\Delta N/\Delta\Omega^*\Delta M$  was normalized by

use of the incident beam flux, the hydrogen target length and density, and the selection procedures described in Sec. III.A.

Besides a correction of the incident beam flux for the beam contamination (see Table I), a second correction was required. This correction, which was on the order of 10%, was necessary to take into account the events which were unmeasurable or ambiguous in some way. These included events that were poorly measured (0.01%), were not measurable due to poor film or poor-quality tracks (2%), or had faulty time-of-flight information (2%), and those in which two tracks ap-

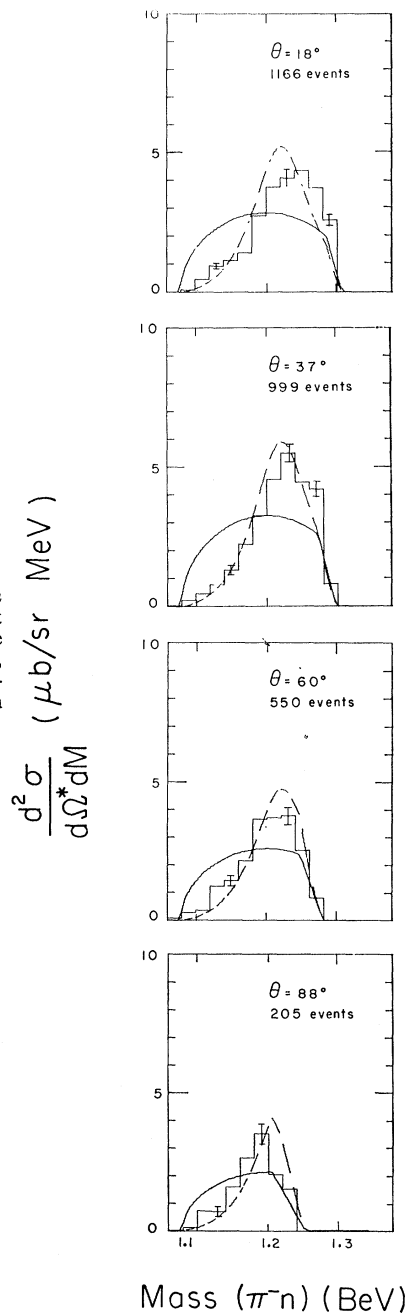


FIG. 8. Our  $\pi^-n$  mass distributions at 516 MeV. Solid curve is phase space, dashed curve is modified resonance form (see text).

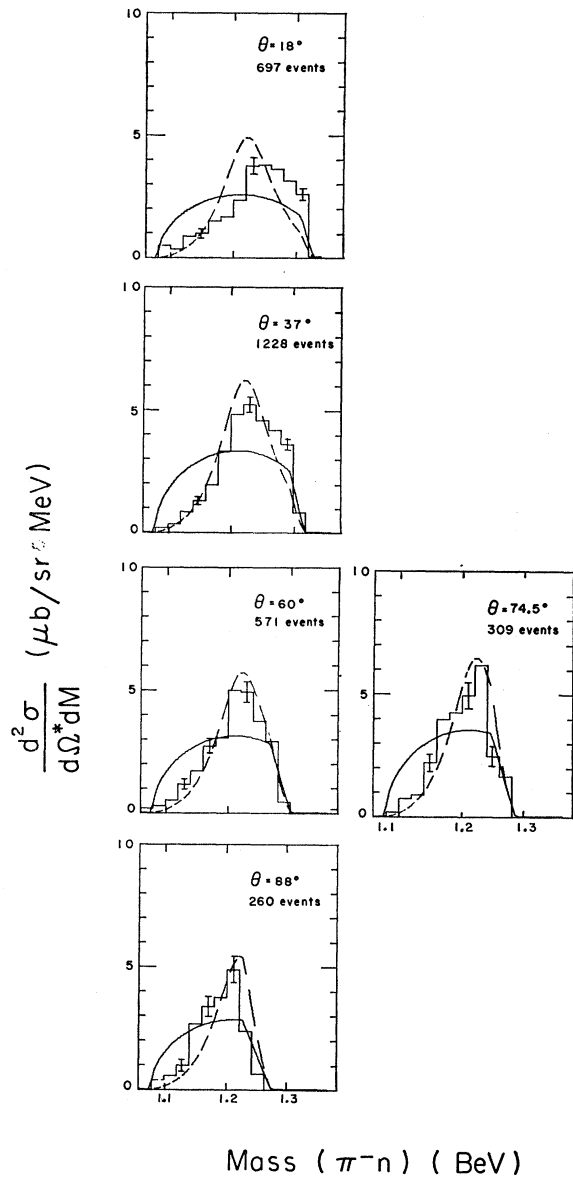


FIG. 9. Our  $\pi^-n$  mass distributions at 550 MeV. Solid curve is phase space, dashed curve is modified resonance form (see text).

peared (2%) or there was no exit track (3%). It was assumed that these events were valid interactions and that they were not of any particular type; thus a direct correction to the number of monitors was made. Events that showed no entrance track (3%) or no tracks at all (3%) were not assumed to be good events, since the entrance spark chamber was very close to 100% efficient; therefore, these were not included in the above correction. The above method of separating the events with missing tracks into those which were valid (for which the monitors were corrected) and those which were spurious (for which the monitors were not corrected) is our best estimate of the real situation.

The final spectra, as functions of  $\pi^-n$  recoil mass, are shown in Figs. 8 through 12 for incident energies from

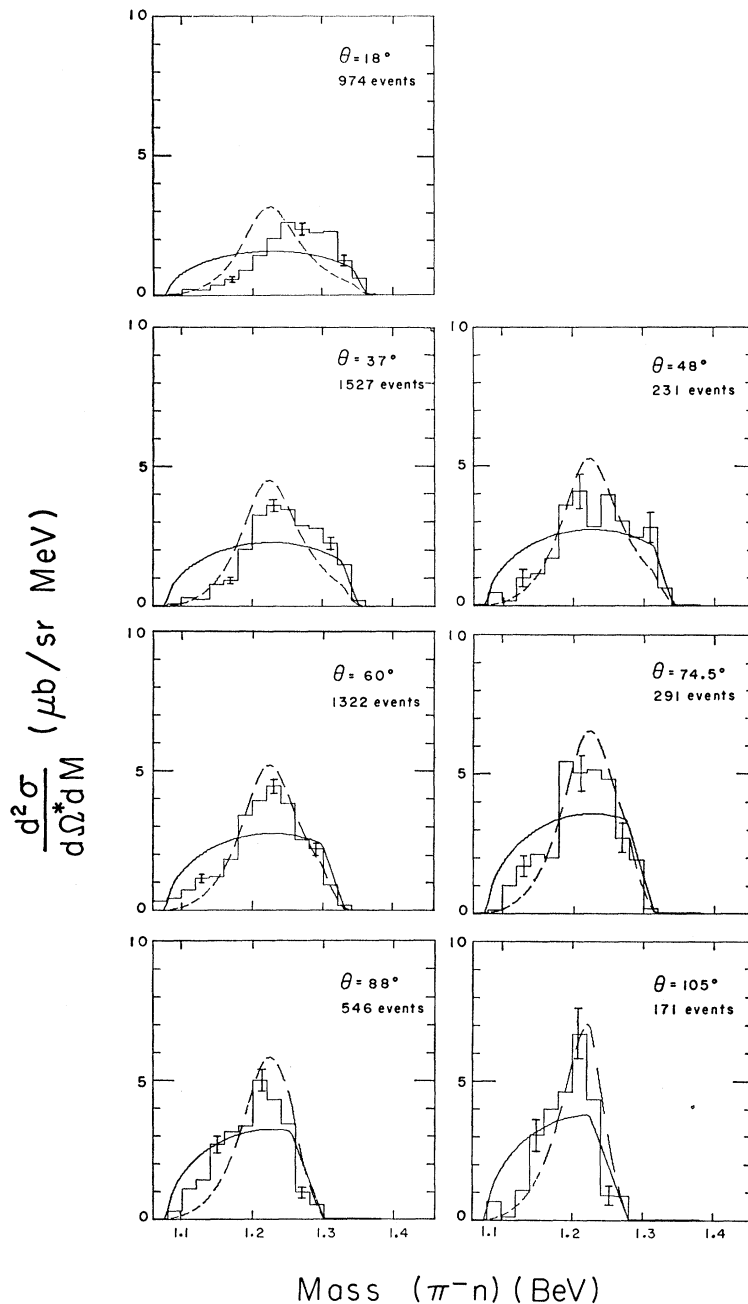


FIG. 10. Our  $\pi^-n$  mass distributions at 599 MeV. Solid curve is phase space, dashed curve is modified resonance form (see text).

515 to 716 MeV. Normalized phase space, as weighted by the spectrometer-efficiency function, is also shown (solid line), as well as a resonance curve (dashed line) for  $N^*$  production, which is discussed in Sec. V. The point at which the spectrometer efficiency drops below 100% can be detected by the "knee" in the phase-space curve.

Error bars are indicated for several points on each histogram. These errors include the statistical error and those associated with the corrections discussed in Sec. III.B. No normalization error is included. The resolution of the spectrometer (see Sec. II), when expressed in terms of  $\pi^-n$  recoil mass, varies from 3 to 15 MeV. Thus, in all cases, the resolution is less than our bin width of 20 MeV.

The spectra at high incident energies (shown separately in Fig. 13; only phase-space curves solid lines are compared with data) were treated as described throughout this paper except for two important points: (a) At these high incident energies, more reactions occur which include a  $\pi^+$  in the final state. It was not possible to correct for these and to isolate the  $\pi^+\pi^-n$  final state. Thus, the spectra presented in Fig. 13 represent *all* final states containing a  $\pi^+$ ; the abscissa is the missing mass.

(b) The minimum pion-proton time separation approaches the resolution of our timing system at the higher momenta available at these high incident energies. Because of this, we estimate that an added

uncertainty of at most 10% exists in the pion spectra. This is not included in the errors indicated in Fig. 13.

As a check on this normalization procedure, the elastic  $\pi^-p$  differential cross sections were calculated from the spectrometer proton data. A comparison with other data<sup>9</sup> is shown in Fig. 14.

## V. DISCUSSION

A number of models have been proposed in an attempt to explain the three-body inelastic reactions. Almost invariably, these models group two of the final-state particles into a single particle which later decays. For the  $\pi\pi N$  final state the situation is particularly complex, since there are strong interactions in all three possible pairings of the final-state particles, but no narrow (i.e., long-lived) resonances that can dominate. The dangers of simplified two-body treatments of the three-particle states have been pointed out,<sup>10</sup> and indeed for the models with which we compared our data directly we were unable to obtain satisfactory agreement. However, it is possible to make some qualitative observations, which are described below.

### A. Peierls Model

The original stimulus for this experiment was the Peierls model,<sup>11</sup> in which it was asserted that the 600-MeV peak in the  $\pi^-p$  total cross section was due to a process that would also cause a peaking of the  $N_{33}^*$  production cross section at 600 MeV. Since our experiment was sensitive to isobar production, the amount of isobar could be computed if the recoiling isobar stood out sufficiently from the background in the  $\pi^+$  energy spectra. It can be seen from Figs. 8 through 13 that production of the  $N_{33}^*$  isobar does occur. It is also apparent that this is not all that is happening in the final state. Since, as we discuss below, we could not obtain a fit to our data, we were unable to extract a quantitative estimate of the amount of  $N_{33}^*$  produced as a function of energy and angle. It is therefore not possible to reach a quantitative conclusion regarding the Peierls model. Finally, we note that the theoretical basis of the Peierls model has been questioned.<sup>12</sup>

### B. Isobar Models

The various so-called isobar models, culminating in that of Olsson and Yodh,<sup>13</sup> group either of the pions with

<sup>9</sup> Jerome A. Helland, Calvin D. Wood, Thomas J. Devlin, Donald E. Hagge, Michael T. Longo, Burton J. Moyer, and Victor Perez-Mendez, Phys. Rev. **134**, B1079 (1964); Philip M. Ogden, Donald E. Hagge, and Jerome A. Helland, *ibid.* **137**, B1115 (1965).

<sup>10</sup> C. Lovelace, Phys. Rev. **135**, B1225 (1964).

<sup>11</sup> Ronald F. Peierls, Phys. Rev. Letters **6**, 641 (1961); S. Mandelstam, J. E. Patton, Ronald F. Peierls, and A. Q. Sarker, Ann. Phys. (N. Y.) **18**, 198 (1962).

<sup>12</sup> C. Goebel, Phys. Rev. Letters **13**, 143 (1964).

<sup>13</sup> R. M. Sternheimer and S. J. Lindenbaum, Phys. Rev. **109**, 1723 (1958); **106**, 1107 (1957); S. Bergia, F. Bonsignori, and A. Stanghellini, Nuovo Cimento **16**, 1073 (1960); M. G. Olsson and G. B. Yodh, Phys. Rev. Letters **10**, 353 (1963); M. Olsson and G. B. Yodh, Phys. Rev. **145**, 1309 (1966); Martin Olsson, Ph.D. thesis, University of Maryland Technical Report No. 379, 1964 (unpublished); G. B. Yodh, University of Maryland Technical Report No. 442, 1965 (unpublished).

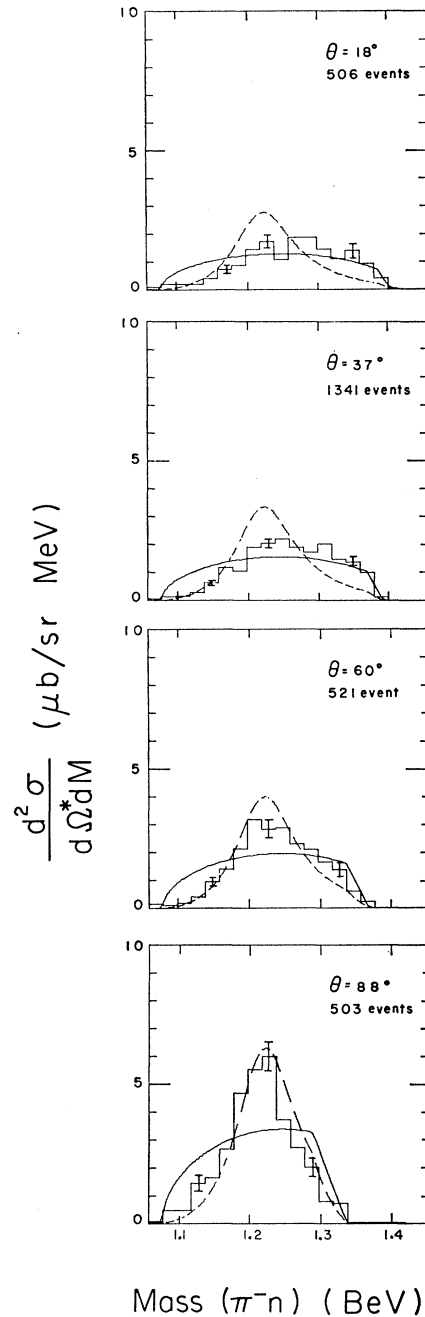


FIG. 11. Our  $\pi^-n$  mass distributions at 667 MeV. Solid curve is phase space, dashed curve is modified resonance form (see text).

the nucleon into the  $N_{33}^*$ , with the other pion recoiling; the  $N_{33}^*$  decays to  $\pi N$  a very short time after the main interaction ( $\approx 10^{-23}$  sec). This model has had considerable success and there is no doubt that production of the  $N_{33}^*$  is important. However, the Olsson and Yodh isobar model does not fit the  $\pi^+\pi^-$  spectrum of  $\pi^-p \rightarrow \pi^+\pi^-n$  as measured by Kirz *et al.*,<sup>14</sup> and Olsson and Yodh state that a  $\pi-\pi$  interaction of some sort is necessary.

<sup>14</sup> Janos Kirz, Joseph Schwartz, and Robert D. Tripp, Phys. Rev. **130**, 2481 (1963).

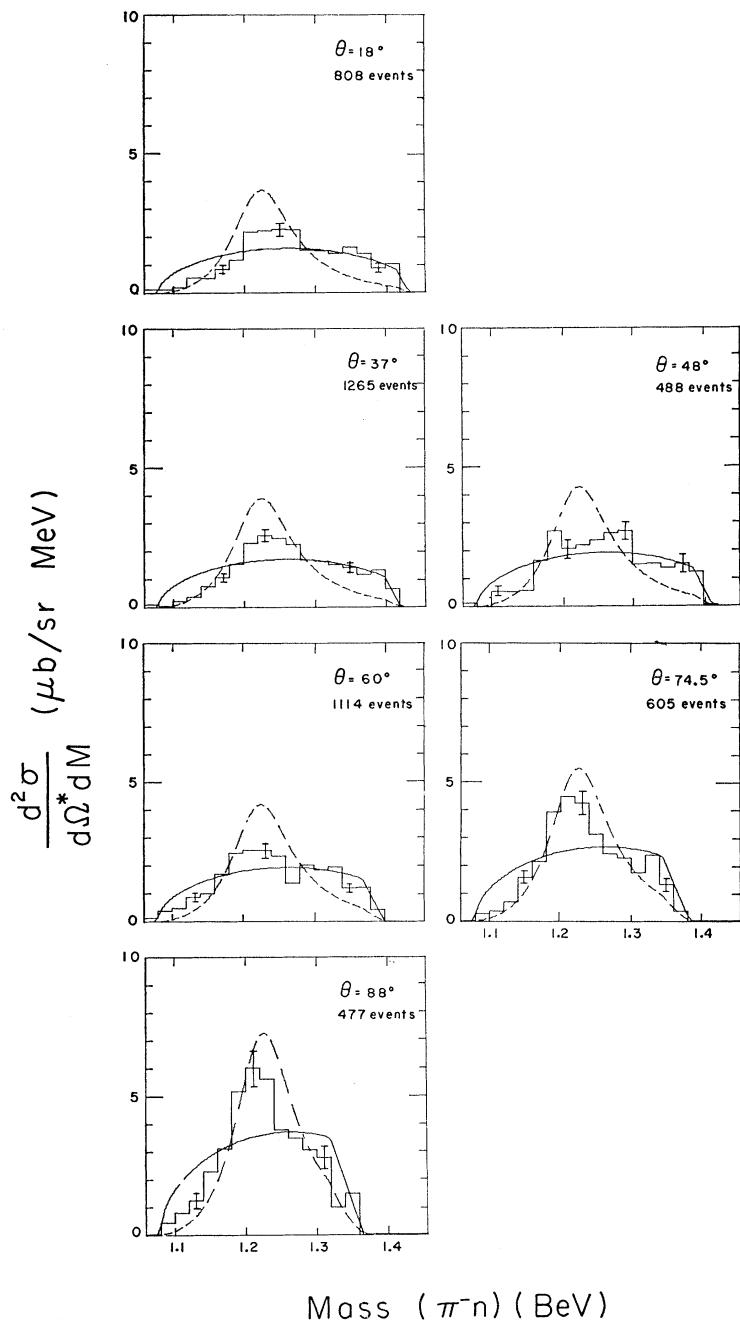


FIG. 12. Our  $\pi^-n$  mass distributions at 715 MeV. Solid curve is phase space, dashed curve is modified resonance form (see text).

Two different isobar models were used to try to fit our spectra. The first was simply an incoherent mixture of phase space plus a resonance form, and the second was the Olsson-Yodh model, which is at present the most sophisticated of the isobar models. In the first case, two different forms were chosen for the resonance shape: (a) the usual Breit-Wigner form,<sup>15</sup> and (b) a resonance form, as discussed by Jackson,<sup>16</sup> which includes certain

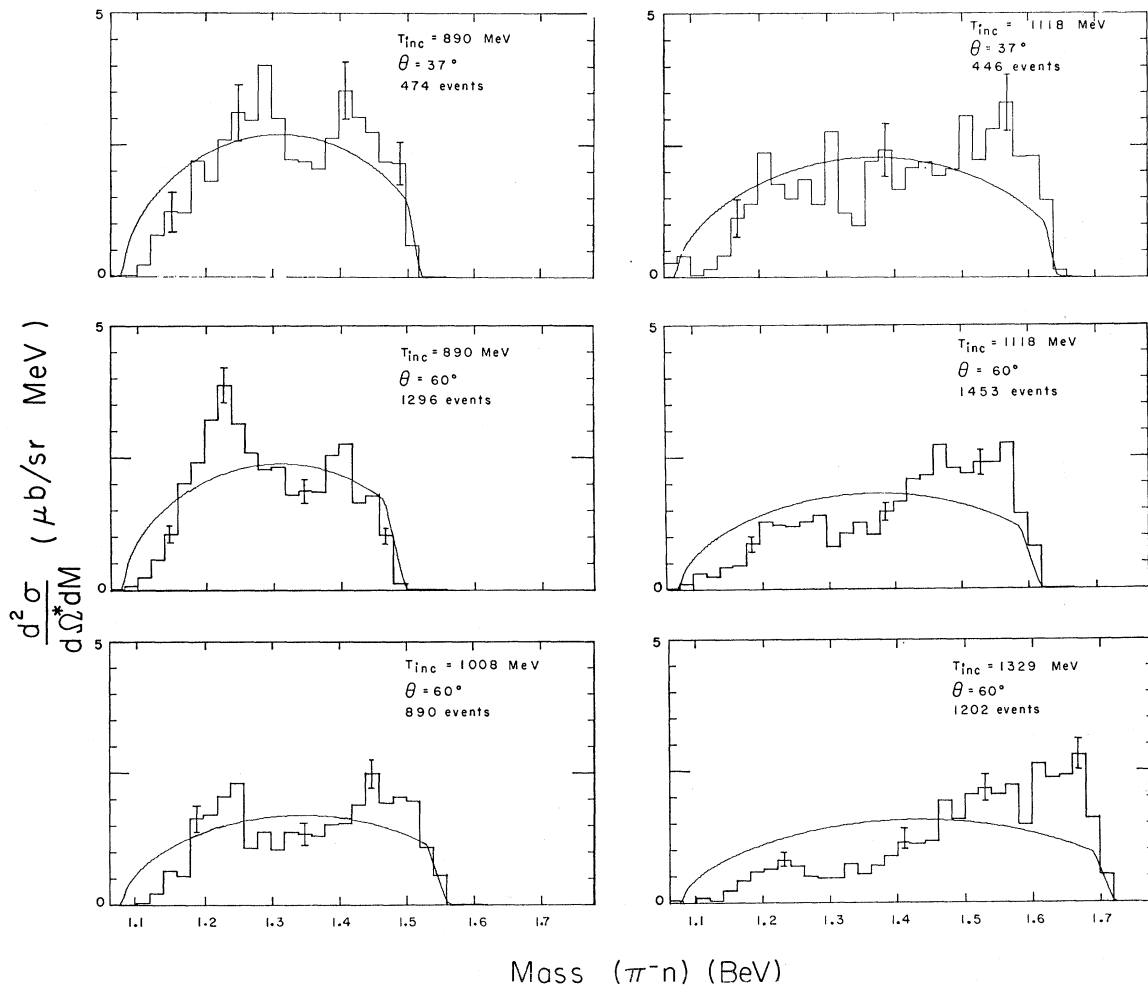
<sup>15</sup> John M. Blatt and Victor F. Weisskopf, *Theoretical Nuclear Physics* (John Wiley & Sons, Inc., New York, 1952), pp. 392-394.

<sup>16</sup> J. D. Jackson, *Nuovo Cimento* **34**, 1644 (1964). The differential distribution is

$$d\sigma \propto d\sigma_s(M) \frac{\Gamma(M) M dM}{(M_0^2 - M^2)^2 + M_0^2 \Gamma^2(M)}$$

shape-distorting factors related to the production of the resonance in a multiparticle final state. On each of the histograms in Figs. 8 through 12 the resonance form given by Jackson is plotted normalized to the total number of events (dashed curves). Note that the center of the peak is shifted slightly from 1238 MeV because of the factor of momentum present in the Jackson form.<sup>16</sup> It was not possible to obtain a good fit in most cases with either resonance form plus three-

where  $M$  is the recoil  $\pi^-n$  mass,  $M_0 = 1238$  MeV,  $\Gamma(M)$  is the energy-dependent  $N^*$  width, and  $d\sigma_s(M)$  is the cross section for  $\pi N \rightarrow \pi N^*$ . We have taken  $d\sigma_s$  proportional to two-body phase space for production in a state of orbital angular momentum  $l$  (i.e.,  $d\sigma_s \propto P^{2l+1}$ ). The curves in Figs. 8 through 12 are for  $l=0$ .


 FIG. 13. Mass distribution of all particles recoiling from  $\pi^+$  in  $\pi^-p$  collisions at the higher incident energies.

body phase space. However, in a few cases, the resonance form alone was able to give fair agreement.

The Olsson and Yodh model<sup>13</sup> includes interference between the two possible formations of the  $N_{33}^*$  isobar (each pion can combine with the nucleon to form the isobar), as well as the  $p$ -wave nature of the isobar decay. In addition, the isobar is allowed to be produced in various angular-momentum states. We were unable to obtain a good representation of our measured distributions with reasonable variations of the parameters that enter in this model, although we must note that the attempt was not exhaustive. A good fit was not obtained for two main reasons: (a) in a number of our spectra there is an excess of events in the high  $\pi^-n$  mass region<sup>17</sup> and, in contrast, a lack of events for low masses of the  $\pi^-n$  system compared with the predictions of the Olsson and Yodh model; and (b) we find that the position of the isobar peak changes slightly as a function of energy and angle, whereas this model predicts that the position of the  $N_{33}^*$  peak remains constant as a function of angle. We are thus led to the

<sup>17</sup> This feature seems to be more pronounced for forward  $\pi^+$  angles, but the spectrometer-efficiency function (see Sec. II) makes it impossible for us to examine this region of the spectrum at large  $\pi^+$  angles.

conclusion that the isobar model is not sufficient to explain the  $\pi^-n$  mass spectra.

### C. Pole Model of Isobar Production

Whereas at the lower incident energies the isobar production seems close to isotropic, our spectra at 599 MeV and above show that there is an increase in isobar production as the  $\pi^+$  angle becomes large (smaller angle of isobar production). Such a production angular distribution is qualitatively consistent with a nucleon-exchange production diagram (Fig. 15). This diagram might also account for the shifting of the isobar peak to lower mass at the more forward production angles, because the pion is emitted only in a  $p$  wave at the lower vertex. Hence, a factor of  $P^3$  would enter the  $\pi^+$  differential cross section<sup>16</sup> and shift the peak to a higher  $\pi^+$  energy (lower  $\pi^-n$  mass).

This nucleon-exchange diagram is included in a model for isobar production in  $\pi-N$  collisions proposed by Selleri.<sup>18</sup> The model also includes contributions from  $\rho$ -meson exchange and from the nucleon pole in the direct channel, but the nucleon-exchange contribution is dominant in the 500–700-MeV region. We have

<sup>18</sup> F. Selleri, *Nuovo Cimento* **37**, 278 (1965); **40A**, 236 (1965).

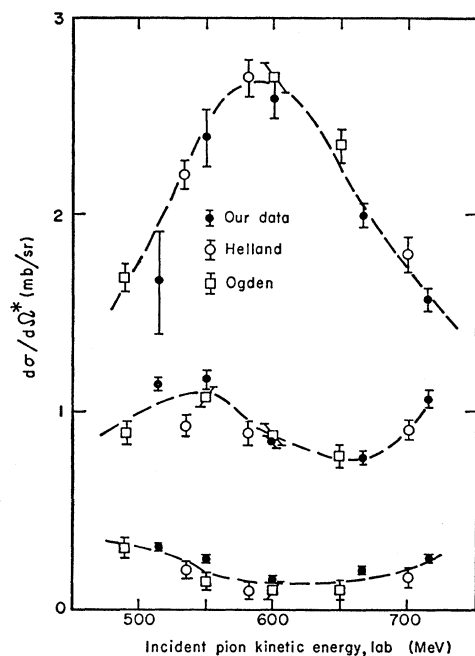


FIG. 14. The  $\pi^-p$  differential cross sections at proton angles of 60 deg (top), 18 deg (center), and 37 deg (bottom) as a function of beam energy. The dashed line is intended only to guide the eye.

calculated the energy spectra, angular distribution, and total cross section according to this model and find the following: (a) the  $\pi^+$  energy spectra are essentially of the same nature as those obtained with the simplest isobar model,<sup>16</sup> and thus the same difficulty with the low-energy portions of the distribution exists as with the isobar models; (b) the production angular distribution (i.e., normalization of the energy spectra) can be made to agree with our data with reasonable values of the model's parameters; and (c) the total cross sections predicted for the other pion-production reactions in  $\pi-N$  collisions in this energy region disagree seriously with measured values.<sup>19</sup> In general, the calculated cross section for the  $\pi N \rightarrow \pi N^*$  shows no peaking in the region of 600 MeV, but simply is an increasing function of the incident energy.

#### D. $\pi-\pi$ Interactions

An additional effect which is expected to contribute to the  $\pi^+$  spectra would be a  $\pi-\pi$  interaction. The  $\pi^+-\pi^-$  system of concern here receives contributions from the  $\pi-\pi$  interactions in the isotopic spin  $T=0, 1$ , and 2 states. We have calculated the  $\pi^+$  spectra resulting from the following assumptions about the interaction in the three isotopic spin states.

The  $T=2$  amplitude is zero. The  $T=1$  amplitude is due only to the  $\rho$  meson and given by a relativistic  $p$ -wave resonance form.<sup>16</sup> Peripheral production of the resonance was used. For the  $T=0$  amplitude the situa-

<sup>19</sup> R. L. Rosenberg and L. D. Roper, Lawrence Radiation Laboratory Report No. UCRL-14202, 1965 (unpublished).

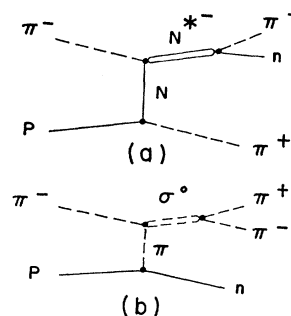


FIG. 15. (a)  $N^*$  production by nucleon exchange. (b) Peripheral production of  $\sigma^0$ .

tion is not clear and hence we tried several possibilities currently being considered:

(a) The  $T=0$  amplitude is due to the  $\sigma$  meson and is given by a relativistic  $s$ -wave resonance form with a mass of 400 MeV and a width of 100 MeV. Both isotropic production of the resonance and peripheral-model production (Fig. 15) were used.

(b) The  $T=0$  amplitude is given by the effective-range expression of Chew and Mandelstam for the case of a dominant  $s$ -wave  $\pi-\pi$  interaction.<sup>20</sup> The scattering length was varied from<sup>21</sup>  $+2.0$  to<sup>22</sup>  $-2.0$  pion Compton wavelengths.

In all cases the  $\pi^+$  spectrum showed no particular peaking at lower energies or depletion at higher energies, as would be required to successfully fit our measured spectra.

These several possibilities for the  $\pi-\pi$  amplitude were also incorporated into the isobar-production model by Selleri discussed in the preceding section. We found that no better agreement with the measured  $\pi^+$  distributions resulted from the combination of  $\pi-\pi$  and nucleon-exchange contributions or the interference between them.

In summary, we find that although  $N_{33}^*$  production is surely present, (a) it alone is not sufficient to explain the data of this experiment, and (b) it plays no obvious role in the peaking of the  $T=\frac{1}{2}$  cross section at 600 MeV in the  $\pi N$  system. Indeed, because of the overlapping effects of the strong interactions in all pairings of the three final-state particles, it is impossible to isolate the  $N_{33}^*$  production from other processes.

#### ACKNOWLEDGMENTS

We would like to thank various members of the staff of the Lawrence Radiation Laboratory for their help and support during the course of this experiment: Professor B. J. Moyer and Professor A. C. Helmholz, Walter Hartsough and the Bevatron crew, Jon Kiiskinen and the other scanners, as well as our colleagues, Dr. Don Lind, Dr. Jim Carroll, and Dr. William Bowman who helped us take data at various times during the run.

<sup>20</sup> G. F. Chew and S. Mandelstam, Phys. Rev. **119**, 467 (1960).

<sup>21</sup> J. Hamilton, P. Menotti, G. C. Oades, and L. L. J. Vick, Phys. Rev. **128**, 1881 (1962).

<sup>22</sup> Geoffrey Chew, Phys. Rev. Letters **16**, 60 (1966).

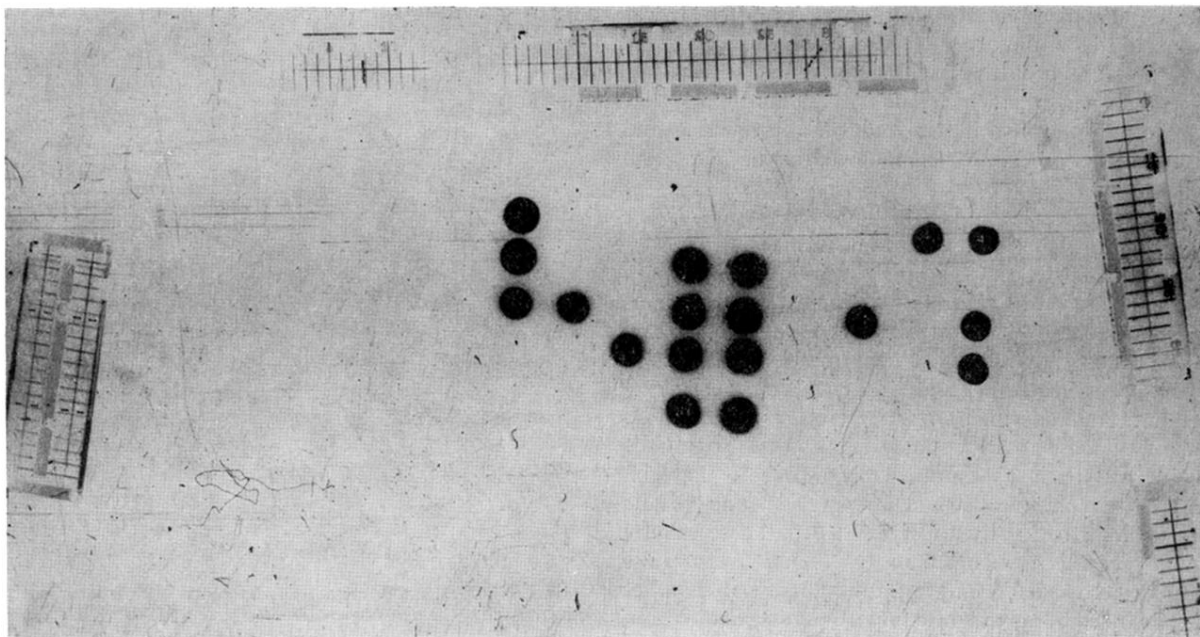


FIG. 4. A typical event photograph of the particle tracks in the spark chambers surrounding the spectrometer magnet. The spark chamber at the left was at the entrance to the magnet. Although the spark chambers were at right angles to one another, on the film they do not appear that way because of the characteristics of our optical mirror system. The large numbered dots in the center are the data box lights, which indicate the frame number, timing information, and  $S_i$  counter number.